

NJC

Accepted Manuscript



This is an *Accepted Manuscript*, which has been through the Royal Society of Chemistry peer review process and has been accepted for publication.

Accepted Manuscripts are published online shortly after acceptance, before technical editing, formatting and proof reading. Using this free service, authors can make their results available to the community, in citable form, before we publish the edited article. We will replace this *Accepted Manuscript* with the edited and formatted *Advance Article* as soon as it is available.

You can find more information about *Accepted Manuscripts* in the [Information for Authors](#).

Please note that technical editing may introduce minor changes to the text and/or graphics, which may alter content. The journal's standard [Terms & Conditions](#) and the [Ethical guidelines](#) still apply. In no event shall the Royal Society of Chemistry be held responsible for any errors or omissions in this *Accepted Manuscript* or any consequences arising from the use of any information it contains.

ARTICLE

Role of Spectator Ions in Influencing the Properties of Dopant-free ZnO Nanocrystals

Cite this: DOI: 10.1039/x0xx00000x

M. Ibrahim Dar,^{a,b} Neha Arora,^c Nagendra Pratap Singh,^b S. Sampath,^c and Srinivasrao A. Shivashankar^{*a,b}Received 00th January 2012,
Accepted 00th January 2012

DOI: 10.1039/x0xx00000x

www.rsc.org/

Towards fundamental studies and potential applications, achieving precise control over the generation of defects in pure ZnO nanocrystals has been always intriguing. Herein, we explored the role of spectator ions (Co²⁺ and Ni²⁺) in influencing the functional properties of ZnO nanocrystals. Crystalline quality, phase purity, and composition of as-prepared samples were thoroughly established by powder X-ray diffraction, electron microscopy (TEM and STEM), and by Raman and X-ray photoelectron spectroscopies (XPS). Despite the presence of Co²⁺ and Ni²⁺ ions in the reaction mixture, STEM-energy dispersive spectroscopy (EDS), XPS analysis, and inductively-coupled plasma mass spectrometry (ICP-MS) revealed that the ZnO nanocrystals formed are dopant-free. Even so, their luminescence and magnetic properties were substantially different from those of pure ZnO nanocrystals synthesized using similar methodology. We attribute the origin of these properties to the defects associated with ZnO nanocrystals generated under different but optimized conditions.

Introduction

Not merely dimensions, morphology, and composition, but the useful properties of nanomaterials are often driven by the defects associated with the nanomaterials; it may indeed be said that “defects define a device”. Thermodynamically, the formation of defects is a given and follows from the negative Gibbs free energy of formation of intrinsic defects.¹ In general, therefore, defects are an integral part of materials, and could be located within the lattice or on the surface of nanomaterials. The higher surface-to-volume ratio in nanomaterials is accompanied by a corresponding increase in unsaturated bonding at the solid-air or solid-liquid interfaces. Such unsaturated bonding leads to enhancement in the overall concentration of surface defects.^{2,3} Various approaches have been adapted to control or induce the defects in semiconductor nanomaterials.^{4,5}

Understanding the nature of these defects becomes important as the presence of such defects dictates the properties of semiconductor nanomaterials. Among various semiconductor nanomaterials, defects in ZnO nanomaterials have been investigated extensively.⁴ In addition to its stability, versatility, and low cost, ZnO nanostructures have been significant because of the variety of defects they can host. These features span a range of possible applications, making ZnO nanostructures the focus of investigations in a wide range of fields, such as ultraviolet laser devices, catalysis, and solar energy harvesting.^{6,7,8}

ZnO is an n-type wide band-gap (3.37 eV) transparent semiconductor. The large exciton binding energy (~ 60 meV) and strong exciton emission impart a stable room temperature

luminescence to the ZnO.⁶ In the literature, there are various reports explaining the origin of luminescence in pure ZnO nanostructures. Owing to quantum confinement and variation in the surface-to-volume ratio, the carrier recombination processes leading to emission depend on size of the ZnO nanomaterial. Fonoberov *et al.*⁹ documented that, in ZnO nanocrystals, the recombination processes are temperature-dependent and accordingly could be either acceptor-bound or donor-bound. In addition to size, the presence and the nature of defects considerably influence properties of ZnO nanostructures such as photoluminescence (PL) and cathodoluminescence (CL).

In the context of dilute magnetic semiconductors (DMS), doped ZnO nanostructures have been studied, theoretically as well as experimentally. Recently, it has been reported that ZnO can exhibit magnetic behavior in the nano-regime.¹⁰ Such ordered magnetic behavior could be attributed to surface defects, which could be pronounced under certain conditions in the nano-regime. Hong *et al.*¹¹ demonstrated that reducing the dimension along the *c*-axis of dopant-free ZnO results in induced magnetism; however, size reduction along the other two axes, *i.e.*, *a* and *b*, brought out no such magnetic behavior.

Herein, we report a simple and facile approach to induce defects in ZnO nanocrystals. Typically, in the presence of non-zinc ions (Co²⁺ or Ni²⁺), nearly monodisperse ZnO nanocrystals were synthesized by sonochemical decomposition of zinc acetylacetonate in ethanolic solution. The formation of dopant-free ZnO (free of Co²⁺ (ZnO-Co) or Ni²⁺ (ZnO-Ni)), its phase purity, and monodispersity were established unambiguously by various analyses. The influence of defects on the functional properties of dopant-free ZnO nanocrystals has been established by recording their room temperature photoluminescence (colloid), cathodoluminescence (solid) and

low temperature magnetism. By controlling defects and thereby photophysical properties using a very simple approach renders the present effort unprecedented.

Results and discussion

ZnO nanocrystals were synthesized in the solution medium through sonochemical decomposition of zinc acetylacetonate in the presence of non-zinc ions (Co^{2+} or Ni^{2+}).

Structural characterization

The crystallinity of the pure ZnO, ZnO-Co and ZnO-Ni nanocrystals is shown clearly by powder XRD (Fig. 1). All observed peaks in the powder XRD patterns can be indexed to the hexagonal wurtzite structure of ZnO (JCPDS No. # 36-1451).

The peaks are broader in ZnO-Co, and the average crystallite size in pure ZnO, ZnO-Co and ZnO-Ni, estimated by applying the Scherrer equation to the most intense peak (101), was found to be 28 nm, 21 nm, and 24 nm, respectively.

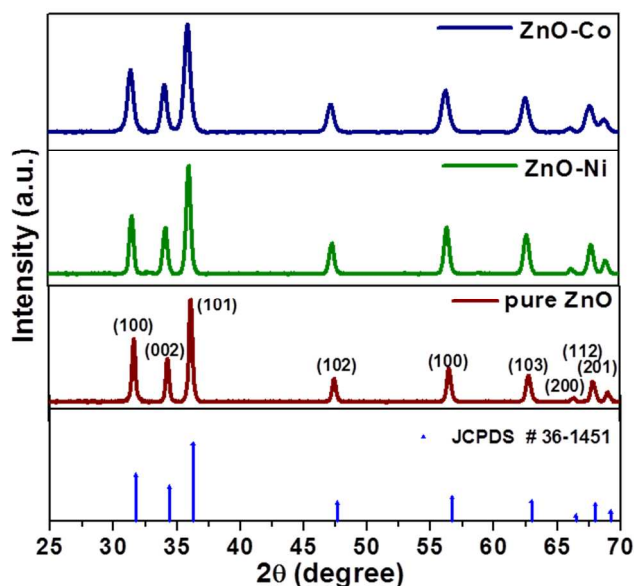


Fig. 1 Powder X-ray diffraction patterns for pure ZnO, ZnO-Co and ZnO-Ni.

The Scherrer formula clearly shows that the as-prepared pure ZnO, ZnO-Co and ZnO-Ni samples comprise very fine hexagonal ZnO nanocrystals. To within the detection limit of XRD, no peak characteristic of the oxides of cobalt or nickel was found in the XRD patterns of ZnO-Co and ZnO-Ni, respectively.

Raman spectral analysis

Fig. 2 shows the Raman spectra of pure ZnO, ZnO-Co, and ZnO-Ni nanocrystals. ZnO exhibits $P6_3mc$ or C_{6v} symmetry and near the center of the Brillouin zone in ZnO, the vibration modes are: A_1 , a doubly degenerate E_1 , two doubly degenerate E_2 and two B_1 modes. $A_1 + E_1 + 2E_2$ are the Raman-active modes in ZnO, where A_1 and E_1 are polar, and split into transverse optical (TO) and longitudinal optical (LO) phonons with different frequencies.¹²

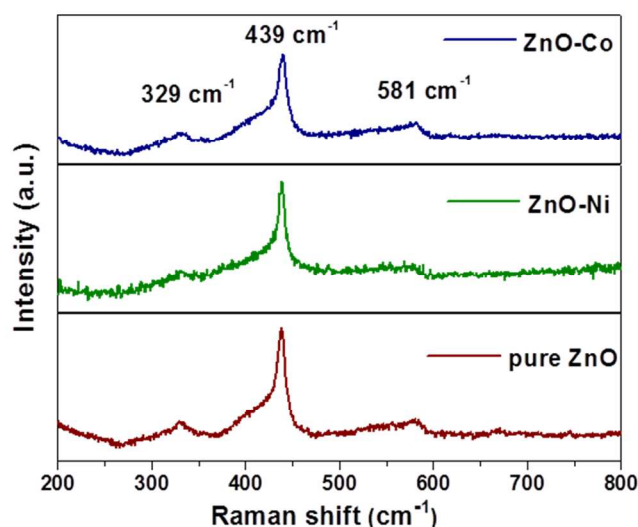


Fig. 2 Raman spectra of pure ZnO, ZnO-Co and ZnO-Ni nanocrystals.

The peak at 439 cm^{-1} corresponds to the E_2 (high) mode, and the peak at 329 cm^{-1} can be assigned to second-order Raman scattering, whereas the peak at 581 cm^{-1} results from the polar symmetry mode that falls between A_1 (LO) and E_1 (LO) modes of ZnO.¹³ The high-intensity peak observed at 439 cm^{-1} (E_2) confirms that the pure ZnO, ZnO-Co and ZnO-Ni nanocrystals are well crystallized. No peak corresponding to the any oxide of cobalt or nickel was observed.

Morphological characterization: electron microscopy

The crystallinity, morphology, size, and dispersion of the ZnO-Co and ZnO-Ni nanocrystals were studied further using transmission electron microscopy (TEM) (Fig. 3). The bright-field TEM micrograph (BF-TEM) of ZnO-Co (Fig. 3a) displays the presence of individual, acicular nanocrystals with an average diameter of 24 nm. A high-resolution image (Fig. 3b) reveals crystal lattice fringes with d spacing of 2.8 Å and 2.5 Å, corresponding to the (100) and (101) plane of hexagonal ZnO, respectively, and are consistent with the corresponding FFT pattern in the inset. Similarly, BF-TEM micrograph of ZnO-Ni (Fig. 3d) features the presence of individual, acicular nanocrystals with an average diameter of 28 nm. A high-resolution image (Fig. 3e) reveals crystal lattice fringes with d spacing of 2.5 Å, corresponding to the (101) plane of hexagonal ZnO, in accordance with the corresponding FFT pattern in the inset. The selected-area electron diffraction (SAED) patterns obtained for ZnO-Co (Fig. 3c) and ZnO-Ni (Fig. 3f) show rings with d spacing that match perfectly with hexagonal ZnO, corroborating the XRD data. The HRTEM reveals that the nanocrystals are well-formed, with the crystals of ZnO-Ni being larger on average than those of ZnO-Co. Such a variation in the particles sizes in ZnO-Co and ZnO-Ni could be attributed to the growth inhibition due to the presence of non-zinc ions, i.e., Co^{2+} or Ni^{2+} in the reaction mixture.

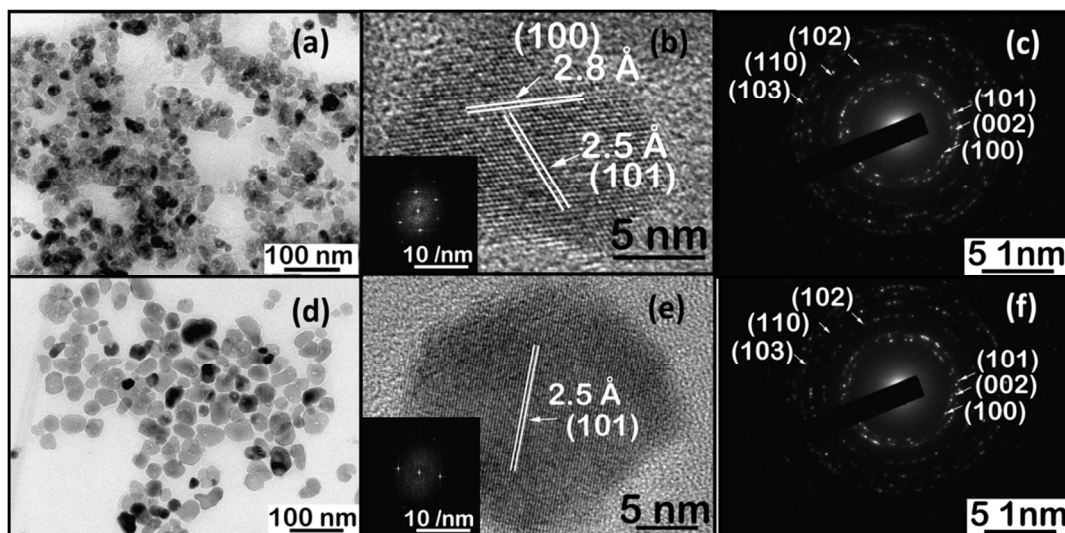


Fig. 3 (a-c) ZnO-Co nanocrystals, (d-f) ZnO-Ni nanocrystals: (a), (d) BFTEM images, (b), (e) HRTEM images (inset: FFT pattern); (c), (f) SAED patterns corresponding to hexagonal ZnO.

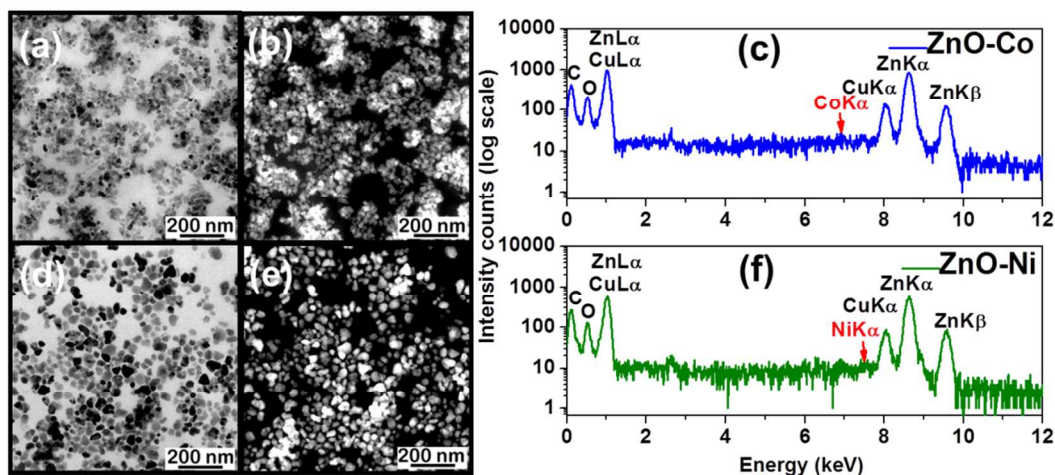


Fig. 4 (a-c) ZnO-Co nanocrystals, (d-f) ZnO-Ni nanocrystals: (a, d) STEM bright-field image; (b, e) STEM dark-field images (c, f) EDS spectra.

Recently, Joo *et al.*¹⁴ reported the synthesis of nanostructured ZnO with rational control over the growth using the hydrothermal method, and documented a classical thermodynamics-based mechanism for growth. These authors explained the underlying growth inhibition by invoking a mechanism of competitive and face-selective electrostatic adsorption of non-zinc ions in a basic medium.

Even though no template or surfactant was employed in the present synthesis, aggregation or agglomeration was not observed, apparently because the low solution temperature limits the mobility gained by the growth species from sonic agitation. As nucleation occurs simultaneously everywhere in the solution subjected to the sonic field, prevention of

aggregation results in the formation of nearly monodisperse nanocrystals.

Dispersion of nanocrystals in ZnO-Co and ZnO-Ni was further analysed by performing scanning transmission electron microscopy (STEM). The bright-field and dark-field imaging under the STEM mode for ZnO-Co (Fig. 4a, b) and ZnO-Ni (Fig. 4d, e) samples corroborated the TEM data. Correspondingly, the formation of well separated nanoparticles in ZnO-Co and ZnO-Ni may be attributed to slow nucleation under low temperature conditions. In addition, STEM-DF micrographs brought out the presence of surface cavities in ZnO nanocrystals, which presumably could be formed due to the etching facilitated by the presence of a strong sonic field.

Elemental analysis

Electron microscopy amply evidenced the formation of nearly monodisperse pure ZnO (ESI), ZnO-Co and ZnO-Ni nanoparticles after sonicating the reaction mixture. As is known, the chemical composition strongly determines the properties of nanostructures. Therefore, energy-dispersive X-ray analysis using the STEM mode and ICP-MS measurements for compositional analysis, and X-ray photoelectron spectroscopy (XPS) for binding energy determination were employed. EDS analysis performed in slow scan in STEM mode (Fig. 4c, f) revealed the absence of Co and Ni ions in ZnO-Co and ZnO-Ni nanocrystals, respectively, as no signal (marked by red arrows) corresponding to cobalt or nickel was detected.

XPS was employed to carry out the core level spectral analysis of our samples. Fig. 5 shows the XPS survey of ZnO-Co (Fig. 5a), ZnO-Ni (Fig. 5b) and pure ZnO (Fig. 5c) samples. In addition, core shell XPS spectra of zinc in ZnO-Co (inset top right; Fig. 5a), ZnO-Ni (inset top right; Fig. 5b) and pure ZnO (inset top right; Fig. 5c) reveal two strong peaks at ~ 1022.30 eV and ~ 1045.43 eV with the spin-orbital splitting of ~ 23.1 eV. The peak positions at 1022.30 eV and 1045.43 eV are in agreement with the binding energies of divalent Zn $2p_{3/2}$ and Zn $2p_{1/2}$, respectively.¹⁵ It is to be noted that no signal corresponding to cobalt or nickel was detected,¹⁶ respectively, in ZnO-Co and ZnO-Ni samples, even after recording high-resolution spectra at energies corresponding to cobalt (inset bottom left; Fig. 5a) or nickel (inset bottom left; Fig. 5b).

Considering both the typical detection limit for EDS (100-1000 ppm) and XPS (1.0-0.1 at.%)^{16b} and the background arising from continuous X-rays, we further verified and ascertained, using ICP-MS analysis, that we had indeed obtained dopant-free ZnO nanocrystals. ICP-MS, with a detection limit of 0.01-10 ppb, has the sensitivity required to detect trace elements in solution and estimate their concentration. ICP-MS of acid-digested, diluted sample solutions of ZnO-Co and ZnO-Ni reconfirmed the absence of Co and Ni ions at different concentration levels, respectively, thus corroborating with EDS and XPS elemental analysis.

The absence of Co and Ni in the lattice or on the surface is thus clearly established. The selection of a "single source precursor" for Zn and O (namely, zinc acetylacetonate), in combination with low pH of the ethanolic solution and mild temperature (maximum temperature = 60 °C), leads one to infer that the incorporation of Co or Ni ions into the ZnO lattice might be infeasible under these conditions. As reported in the literature, for the precipitation of Co or Ni ions from the solution (for incorporation into ZnO), a strong alkaline medium or compelling reaction conditions, i.e., high temperature and pressure are required.¹⁷

Effect of defects on the magnetic properties of dopant-free ZnO nanocrystals

Bulk ZnO being diamagnetic, the incorporation of a magnetic dopant such as Co, Fe, or Ni into the ZnO lattice makes it imperative to examine whether the resulting sample is a DMS. Dietl *et al.*¹⁸ reported room temperature ferromagnetism in M^{2+} -substituted ZnO semiconductor ($M = 3d$ elements).

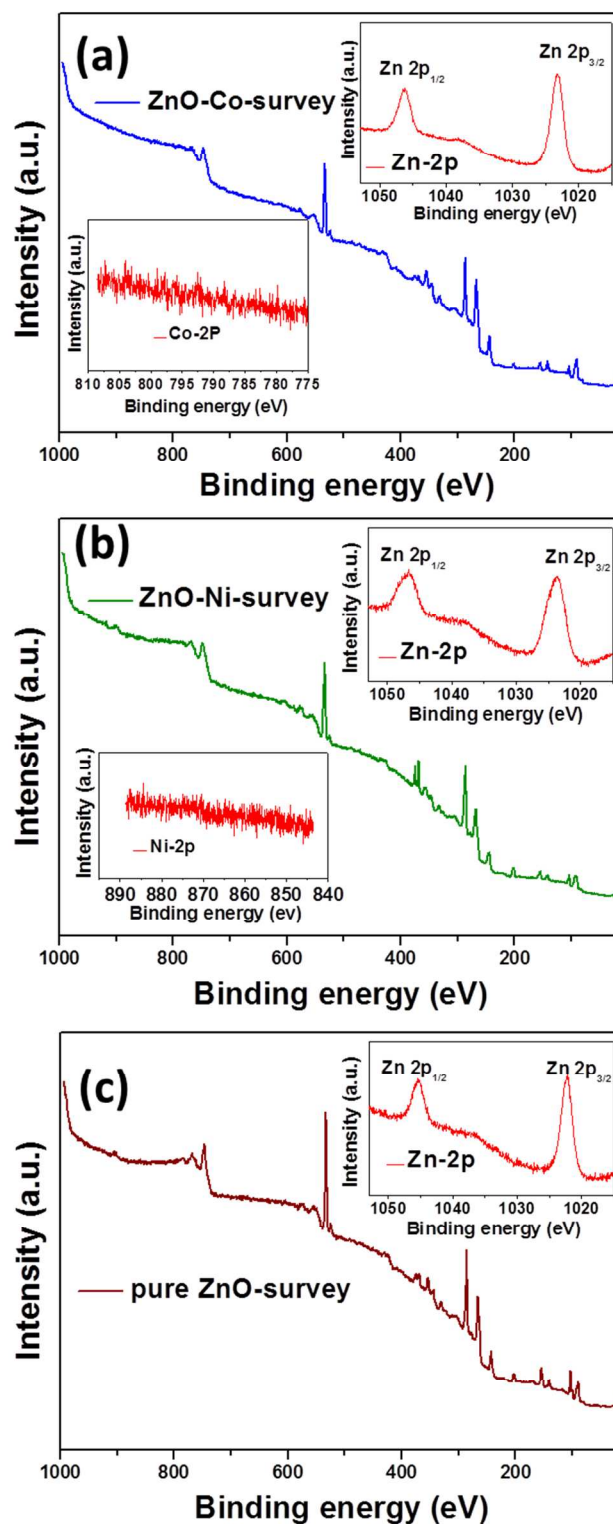


Fig. 5 XPS survey of ZnO-Co, ZnO-Ni and pure ZnO samples, insets; core shell Zn2p spectra of ZnO-Co, ZnO-Ni and pure ZnO nanocrystals, and high-resolution Co-2p and Ni-2p XPS spectra obtained, respectively, from ZnO-Co and ZnO-Ni samples.

Nevertheless, the interpretation of the magnetic properties in DMS-ZnO is considered highly controversial.^{19,20} In addition to doping, the presence of defects associated with ZnO nanocrystals influence their magnetic properties considerably.

Mostly, the observed magnetic behaviour reveals a strong dependence on the ordering of dopant and defects, and on the synthesis methodology.^{21,22,23,24,25,26,27}

Hong *et al.*¹¹ established the significance of shape anisotropy, apart from the effect of size in ZnO nanomaterial on its magnetic behavior. They showed, theoretically as well as experimentally, that the electronic bands formed from the oxygen (2p) and zinc (3d) levels split in 5-8 nm-thick ZnO nanoplates, thereby giving rise to magnetism in dopant-free ZnO nanoplates. Furthermore, Xu *et al.*²⁸ summarized that controlling defects in the ZnO provides a dependable way to obtain reproducible intrinsic, homogeneous ferromagnetism at room temperature. Field-dependent magnetic measurements made on pure ZnO, ZnO-Co and ZnO-Ni nanocrystals at 2 K indicate paramagnetic behavior (Fig 6). Additionally these measurements revealed that magnetization depends strongly on the presence of non-zinc ions, i.e., Co^{2+} and Ni^{2+} , in the reaction mixture during the synthesis.

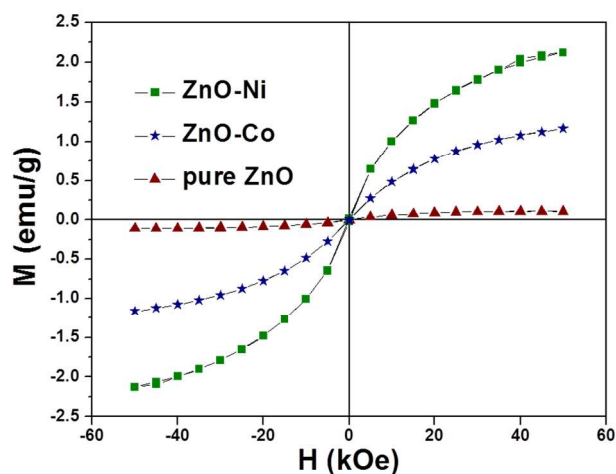


Fig. 6 Magnetic study of pure ZnO, ZnO-Co and ZnO-Ni nanocrystals: Field-dependent magnetization measured at 2 K.

The magnetization saturated at a field of 50 kOe, attaining at 2 K a maximum value (M_{max}) of 0.2 emu/g, 1.1 emu/g, and 2.1 emu/g, respectively, for pure ZnO, ZnO-Co, and ZnO-Ni nanoparticles. The magnitude of magnetic moment observed above is significantly larger than the magnetic moment arising from the unsaturated bonds (10^{-3} emu/g) or from vacancies associated with the surface of pure ZnO nanoparticles, or measured in polycrystalline thin films containing nanocrystals.^{29,30} The magnetic behavior observed in ZnO-Co and ZnO-Ni could be attributed to defects, which were pronounced under optimized conditions in the nano-regime

Effect of defects on the luminescence in dopant-free ZnO nanocrystals

ZnO exhibits stable luminescence at room temperature and the carrier recombination processes leading to emission vary considerably with the dimension of the ZnO nanomaterial. Fonoberov *et al.*⁹ investigated the recombination processes in 4 nm ZnO quantum dots, 20 nm ZnO nanocrystals, and in a reference bulk ZnO sample, with a large number of acceptor defects on the surface. From comparative analysis, they suggested that the PL emission in ZnO quantum dots originates in the recombination of acceptor-bound excitons and remains independent of temperature. However, in ZnO nanocrystals, the recombination could be either acceptor-bound or donor-bound, depending on the temperature.

In addition to size, defects associated with ZnO nanocrystals influence their luminescence properties considerably, just as they do magnetic behavior. A typical PL spectrum of ZnO reveals a feature at about 380 nm, which could be attributed to free exciton recombination through exciton-exciton collisions,⁹ corresponding to the near-band-gap emission (NBE), as well as a broad peak over the visible region. Fig. 7 shows the PL spectra of pure ZnO, ZnO-Co, and ZnO-Ni nanocrystals dispersed in ethanol. The general features of the PL spectra are in good agreement with reports in the literature on ZnO nanostructures.⁹ The broad emission peak is associated with the various deep-level defects, such as zinc vacancy (V_{Zn}), oxygen vacancy (V_{O}), zinc interstitial (Zn_i), oxygen interstitial (O_i) and single-ionized oxygen vacancies in ZnO.³¹⁻³³ To explain these emissions, different hypotheses have been reported; nevertheless, the origin of these emissions remains debatable. The green emission is understood to be due to the recombination of electrons in singly-occupied oxygen vacancies (V_{O}^*) with photoexcited holes in the valence band.³¹ Lin *et al.*³² proposed that emission in the blue is due to singly-ionized deep donor levels (V_{O}), and that yellow emission may be due to deep acceptors (O_i), and not due to shallow acceptors (V_{Zn} and O_{Zn}). Djuricic *et al.*³³ attributed the origin of orange and red emission to defects associated with excess oxygen.

Comparative analysis of PL spectra (Fig. 7) shows that the strongest broad-band emission (BBE) is from ZnO-Ni nanocrystals, followed by ZnO-Co nanocrystals, which further confirms the formation of dopant-free ZnO nanocrystals. As documented,³⁴ the dopant cations quench emission by providing alternate competitive pathways for recombination, thereby diminishing the intensity of BBE. Apparently, nanocrystals with a larger concentration of defects are known to have stronger BBE than NBE.³⁵ The variation in the BBE intensities of ZnO, ZnO-Co, and ZnO-Ni nanocrystals conveys that emission due to defects could be tuned by simply changing the ambiance around nanocrystals during their formation, without altering their chemical composition.

To gain further insight into the impact of defects on the optical properties of zinc oxide nanocrystals, cathodoluminescence measurements were made. Owing to its high sensitivity, cathodoluminescence is considered a versatile technique in understanding point defects in semiconductors.^{36,37}

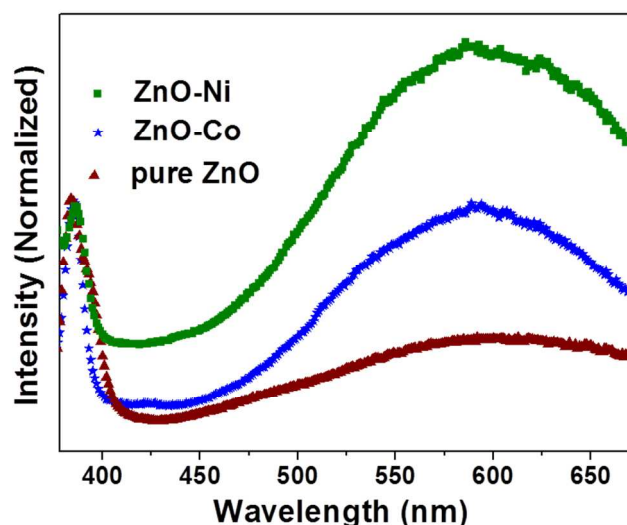


Fig. 7 Room temperature photoluminescence (colloid) of pure ZnO, ZnO-Co and ZnO-Ni nanocrystals.

As shown in Fig. 8, the general features of the CL spectra are in accord with those of room temperature photoluminescence spectra. Similar to PL, cathodoluminescence spectra show near-band-gap emission at about 380 nm attributable to free exciton recombination through exciton-exciton collisions, and the BBE peaking at 570 nm, which can be attributed to emissions related to the various deep-level defects in ZnO. Xi *et al.*³⁶ attributed the green emission in cathodoluminescence to oxygen vacancies and blue emission to transitions from the conduction band and valence band to acceptor levels and donor levels, respectively. Doust *et al.*³⁷ used depth-resolved cathodoluminescence spectroscopy to investigate the distribution of different defects in ZnO crystals. Furthermore, the observed difference in the CL intensities could be explained on the basis of defects, *not dopants*, as the presence of dopant would have led to the quenching of luminescence.

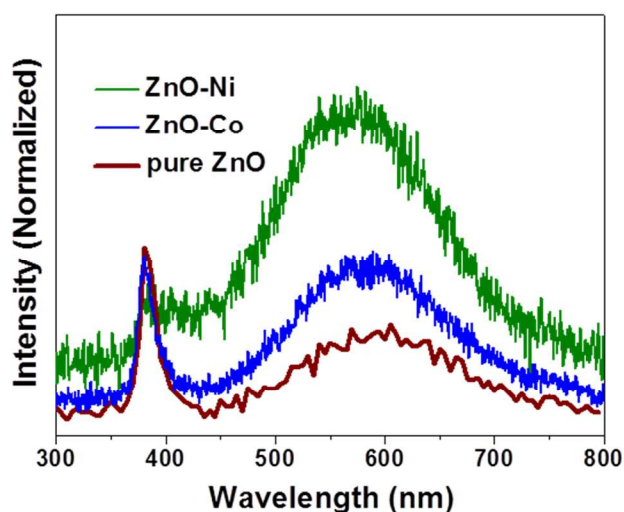


Fig. 8 Room temperature cathodoluminescence (solid) of pure ZnO, ZnO-Co and ZnO-Ni nanocrystals.

Conclusions

In summary, we have taken advantage of the mild conditions of sonochemical synthesis to obtain nearly monodisperse ZnO nanocrystals of dimension less than 30 nm, without incorporating the “spectator ions” of Ni and Co into the lattice. Despite the presence of Co^{2+} and Ni^{2+} ions in the reaction mixture, energy dispersive spectroscopy (EDS), ICP-MS, and XPS analyses showed clearly that the ZnO nanocrystals formed are dopant-free. The observed variation in the intensity of broad-band emission from ZnO nanocrystals conveys that emission due to defects could be tuned by simply changing the ambience around nanocrystals during their formation, without altering their chemical composition. Achieving such control over photophysical properties by tuning defects using a very simple approach renders the present effort novel. For this reason, understanding the mechanism involved becomes imperative and investigations in this direction are under way in our group.

Experimental section

Materials and sonochemical setup

Zinc acetylacetonate anhydrate (Merck) and HPLC-grade absolute ethanol (Commercial Alcohols, Brampton, Ontario) were used for the reaction. $\text{Co}(\text{NO}_3)_2 \cdot 6\text{H}_2\text{O}$ and $\text{Ni}(\text{NO}_3)_2 \cdot 6\text{H}_2\text{O}$ were purchased from S. D. Fine Chemical Limited. All the chemicals of analytical grade were used as-received, without further purification. An ultrasonic processor (SONIC Model VCX 500) operating at 20 kHz, equipped with a solid Ti probe (13 mm diameter), was used in the synthesis, while the amplitude of ultrasonic wave was selected as 50% of the maximum, with a duty cycle of 60%.

Synthesis of ZnO nanocrystals

ZnO nanocrystals were synthesized sonochemically from the complex zinc acetylacetonate. In a typical experiment, 1.98 g of anhydrous zinc acetylacetonate (Merck) and 0.146 g weight per cent of $\text{Co}(\text{NO}_3)_2 \cdot 6\text{H}_2\text{O}$ or $\text{Ni}(\text{NO}_3)_2 \cdot 6\text{H}_2\text{O}$ were dissolved in 80 mL of ethanol (HPLC-grade). The resulting reaction mixtures were sonicated for 15 min with the vessel placed in an ice bath, followed by sonication for 15 min without the ice bath. For comparative analysis, pure ZnO nanocrystals were synthesized using a similar method without adding cobalt or nickel salts.

Isolation and purification of powder

Following sonication, the precipitate was separated from the supernatant by centrifugation at 4000 rpm for 20 min. The precipitate was washed twice with ethanol, followed by drying under ambient conditions. No size-selective precipitation was carried out. The samples obtained in the ambience of $\text{Co}(\text{NO}_3)_2 \cdot 6\text{H}_2\text{O}$ and $\text{Ni}(\text{NO}_3)_2 \cdot 6\text{H}_2\text{O}$ are designated as ZnO-Co and ZnO-Ni, respectively.

Analysis and measurements

Bright-field transmission electron microscopy images (BFTEM), high-resolution electron microscopy (HRTEM) images, selected-area electron diffraction (SAED) patterns, energy-dispersive-X-ray spectroscopy (EDS), and scanning transmission electron microscopy-elemental mapping (STEM-EDS) images of nanocrystals were collected using a JEOL JEM-2100F operating at an accelerating voltage of 200 kV, equipped with an Oxford energy-dispersive X-ray (EDX)

detector. The TEM specimens were prepared by slow evaporation of 20 μL diluted solutions obtained by the dispersion of powder samples in ethanol, deposited on formvar-coated copper grid. Powder X-ray diffraction data were collected on a Bruker Advance D8 X-ray diffractometer with a graphite monochromator, using $\text{Cu K}\alpha$ ($\lambda = 0.154 \text{ nm}$) radiation, at a scanning rate of 0.2 deg min^{-1} . X-ray photoelectron spectra (XPS) were recorded by employing $\text{Mg K}\alpha$ X-rays as the source ($h\nu = 1253.437 \text{ eV}$) (Thermo Scientific Multilab 2000 XPS system). A quadrupole inductively-coupled plasma mass spectrometer (ICPMS, Thermo X Series II) was used for determination of element concentrations. ICP-MS samples were prepared by dissolving 5 mg of the pure ZnO, ZnO-Co, and ZnO-Ni solid nanoparticles using 2% nitric acid solution. The diluted solutions were analysed for Zn, Co, and Ni cation content. Each sample was analysed in triplicate.

Optical absorption and photoluminescence data were collected at room temperature using a Perkin Elmer Lambda 700 UV-vis-near-IR spectrophotometer with a double monochromator optical system. Photoluminescence (PL) spectra of ZnO, ZnO-Co, and ZnO-Ni nanocrystals were obtained with excitation at 360 nm using a xenon lamp. Cathodoluminescence (CL) spectra of ZnO, ZnO-Co, and ZnO-Ni nanocrystals were obtained with ULTRA 55, field-emission scanning electron microscope (Carl Zeiss) with Mono, using voltage of 20 kV and current of 300 nA. Raman spectra of the samples were obtained at room temperature (on a LabRAM HR (UV) instrument), using an argon ion laser (514 nm), with acquisition time 10 sec and a 50x long working distance objective (LMPlanFL N 50x/0.5) to record the data. The magnetic measurements were carried out on powder samples (8-10 mg) using a superconducting quantum interference device (SQUID) magnetometer (Quantum Design MPMS XL-5).

Acknowledgements

M.I.D. thanks the UGC for a fellowship. We thank the Institute Nanoscience Initiative (IISc.) for allowing us to access the microscopy facilities, and the Micro and Nano Characterization Facility (MNCF) located at CeNSE, IISc, (funded by NPMAS-DRDO and MCIT, Government of India) for various analyses.

Notes and references

^a Centre for Nano Science and Engineering, Indian Institute of Science, Bangalore 560012, India. E-mail: shivu@cense.iisc.ernet.in; Fax: +91 80 2360 4656; Tel: +9180 2293 3323

^b Materials Research Centre, Indian Institute of Science, Bangalore 560012, India.

^c Department of Inorganic & Physical Chemistry, Indian Institute of Science, Bangalore 560012, India.

Electronic Supplementary Information (ESI) available: TEM image of pure ZnO, UV-visible absorption spectra of ZnO-Co and ZnO-Ni nanocrystals. See DOI: 10.1039/b000000x/

- 1 A. R. West, *Basic Solid State Chemistry*, 2nd ed.; John Wiley and Sons: New York, 1999.
- 2 R. L. Penn and J. F. Banfield, *Science*, 1998, **281**, 969-971.
- 3 R. L. Penn, *J. Phys. Chem. B*, 2004, **108**, 12707-12712.
- 4 (a) A. B. Djurišić, A. M. C. Ng and X. Y. Chen, *Progress in Quantum Electronics*, 2010, **34**, 191-259. (b) X. H. Huang, Z. Y. Zhan, K. P. Pramoda, C. Zhang, L. X. Zheng and S. J. Chua,

- CrystEngComm*, 2012, **14**, 5163-5165. (c) X. H. Huang, C. Zhang, C. B. Tay, T. Venkatesan, and S. J. Chua, *Appl. Phys. Lett.*, 2013, **102**, 111106-1-111106-3. (d) X. Huang, G. Li, B. Cao, M. Wang, and C. Hao, *J. Phys. Chem. C*, 2009, **113**, 4381-4385.
- 5 C. Zhang and J. Lin, *Chem. Soc. Rev.*, 2012, **41**, 7938-7961.
 - 6 M. H. Huang, S. Mao, H. Feick, H. Yan, Y. Wu, H. Kind, E. Weber, R. Russo and P. Yang, *Science*, 2001, **292**, 1897-1899.
 - 7 Z. R. Tian, J. A. Voigt, J. Liu, B. McKenzie, M. J. McDermott, M. A. Rodriguez, H. Konishi and H. Xu, *Nat Mater*, 2003, **2**, 821-826.
 - 8 M. Law, L. E. Greene, J. C. Johnson, R. Saykally and P. Yang, *Nat Mater*, 2005, **4**, 455-459.
 - 9 V. A. Fonoberov, K. A. Alim, A. A. Balandin, F. Xiu and J. Liu, *Phys. Rev. B*, 2006, **73**, 1653171-1-165317-9.
 - 10 A. Sundaresan, R. Bhargavi, N. Rangarajan, U. Siddesh and C. N. R. Rao, *Phys. Rev. B*, 2006, **74**, 161306-1-161306-4
 - 11 J.-I. Hong, J. Choi, S. S. Jang, J. Gu, Y. Chang, G. Wortman, R. L. Snyder and Z. L. Wang, *Nano Lett.*, 2012, **12**, 576-581.
 - 12 T. C. Damen, S. P. S. Porto and B. Tell, *Phys. Rev.*, 1966, **142**, 570-574.
 - 13 K. A. Alim, V. A. Fonoberov, M. Shamsa, A. A. Balandin, *Appl. Phys. Lett.* 2005, **97**, 124313-1-124313-5.
 - 14 J. Joo, B. Y. Chow, M. Prakash, E. S. Boyden and J. M. Jacobson, *Nat Mater.*, 2011, **10**, 596-601.
 - 15 (a) J. F. Moulder, W. F. Stickle, P. E. Sobol and K. D. Bomben, *Handbook of X-ray Photoelectron Spectroscopy*, Physical Electronics, Eden Prairie, 1995. (b) M. N. Islam, T. B. Ghosh, K. L. Chopra and H. N. Acharya, *Thin Solid Films*, 1996, **280** 20-25.
 - 16 N. S. McIntyre and M. G. Cook, *Anal. Chem.*, 1975, **47**, 2208-2213. (b) A. G. Shard *Surf. Interface Anal.* 2014, **46**, 175-185
 - 17 I. Djerdj, G. Garnweitner, D. Arcon, M. Pregelj, Z. Jaglicic and M. Niederberger, *J. Mater. Chem.*, 2008, **18**, 5208-5217.
 - 18 T. Dietl, H. Ohno, F. Matsukura, J. Cibert and D. Ferrand, *Science*, 2000, **287**, 1019-1022.
 - 19 R. Boubekri, Z. Beji, K. Elkabous, F. Herbst, G. Viau, S. Ammar, F. Fiévet, H. J. von Bardeleben and A. Mauger, *Chem. Mater.*, 2009, **21**, 843-855.
 - 20 Z. Jin, T. Fukumura, M. Kawasaki, K. Ando, H. Saito, T. Sekiguchi, Y. Z. Yoo, M. Murakami, Y. Matsumoto, T. Hasegawa and H. Koinuma, *Appl. Phys. Lett.*, 2001, **78**, 3824-3826.
 - 21 Lawes, A. S. Risbud, A. P. Ramirez and R. Seshadri, *Physical Review B*, 2005, **71**, 045201-1-045201-5
 - 22 Y. D. Park, A. T. Hanbicki, S. C. Erwin, C. S. Hellberg, J. M. Sullivan, J. E. Mattson, T. F. Ambrose, A. Wilson, G. Spanos and B. T. Jonker, *Science*, 2002, **295**, 651-654.
 - 23 K. Ando, *Appl. Phys. Lett.*, 2003, **82**, 100-102.
 - 24 P. Sharma, A. Gupta, K. V. Rao, F. J. Owens, R. Sharma, R. Ahuja, J. M. O. Guillen, B. Johansson and G. A. Gehring, *Nat Mater*, 2003, **2**, 673-677.
 - 25 T. Fukumura, Z. Jin, M. Kawasaki, T. Shono, T. Hasegawa, S. Koshihara and H. Koinuma, *Appl. Phys. Lett.*, 2001, **78**, 958-960.
 - 26 D. C. Kundaliya, S. B. Ogale, S. E. Lofland, S. Dhar, C. J. Metting, S. R. Shinde, Z. Ma, B. Varughese, K. V. Ramanujachary, L. Salamanca-Riba and T. Venkatesan, *Nat Mater*, 2004, **3**, 709-714.
 - 27 A. S. Risbud, N. A. Spaldin, Z. Q. Chen, S. Stemmer and R. Seshadri, *Phys. Rev. B*, 2003, **68**, 205202-1-205202-7
 - 28 Q. Xu, H. Schmidt, S. Zhou, K. Potzger, M. Helm, H. Hochmuth, M. Lorenz, A. Setzer, P. Esquinazi, C. Meinecke and M. Grundmann, *Appl. Phys. Lett.*, 2008, **92**, 082508-1- 082508-3.
 - 29 C. Madhu, A. Sundaresan and C. N. R. Rao, *Phys. Rev. B*, 2008, **77**, 201306-1- 201306-4.
 - 30 B. B. Straumal, A. A. Mazilkin, S. G. Protasova, A. A. Myatiev, P. B. Straumal, G. Schütz, P. A. van Aken, E. Goering and B. Baretzky, *Phys. Rev. B*, 2009, **79**, 205206-1-205206-6.
 - 31 K. Vanheusden, W. L. Warren, C. H. Seager, D. R. Tallant, J. A. Voigt and B. E. Gnade, *J. Appl. Phys.*, 1996, **79**, 7983-7990.
 - 32 Y.-J. Lin, C.-L. Tsai, Y.-M. Lu and C.-J. Liu, *J. Appl. Phys.*, 2006, **99**, 093501-1-093501-4.
 - 33 A. B. Djurišić, Y. H. Leung, K. H. Tam, L. Ding, W. K. Ge, H. Y. Chen and S. Gwo, *Appl. Phys. Lett.*, 2006, **88**, 103107-1- 103107-3.
 - 34 B. Panigrahy, M. Aslam and D. Bahadur, *J. Phys. Chem. C*, 2010, **114**, 11758-11763.

- 35 M. I. Dar, S. Sampath and S. A. Shivashankar, *Mater. Res. Express*, 2014, **1**, 015025.
- 36 F. Zhu-Xi, G. Chang-xin, L. Bi-xia, L. Gui-Hong, *Chin. Phys. Lett.*, 1998, **15**, 457-459.
- 37 D. Doult, H. L. Mosbacker, G. Cantwell, J. Zhang, J. J. Song and L. J. Brillson, *Appl. Phys. Lett.*, 2009, **94**, 042111-1- 042111-3.